Ultrathin porous graphitic carbon nitride from recrystallized precursor toward significantly enhanced photocatalytic water splitting

Cheng Cheng [a,b], Jinwen Shi [a,c,*], Liuhao Mao [a], Chung-Li Dong [d], Yu-Cheng Huang [d], Shichao Zong [a], Jiamei Liu [e], Shaohua Shen [a], Liejin Guo [a]

[a] International Research Center for Renewable Energy (IRCRE), State Key Laboratory of Multiphase Flow in Power Engineering (MFPE), Xi'an Jiaotong University (XJTU), 28 West Xianning Road, Xi'an 710049, China
[b] School of Chemical Engineering and Technology, Xi'an Jiaotong University (XJTU), 28 West Xianning Road, Xi'an 710049, China
[c] Integrated Energy Institute, Sichuan Digital Economy Industry Development Research Institute, 88 Jiefang Road, Chengdu 610036, China
[d] Department of Physics, Tamkang University, 151 Yingzhuan Road, Tamsui 25137, Taiwan, China
[e] Instrumental Analysis Center of Xi'an Jiaotong University, Xi'an Jiaotong University (XJTU), 28 West Xianning Road, Xi'an 710049, China

HIGHLIGHTS

- Hydrothermal treatment induced biuret recrystallization to form biuret hydrate with regular morphology and large crystal size.
- Biuret hydrate as precursor promoted the thermal polymerization of melem for the formation of graphitic carbon nitride (BCN-HT100) network.
- The obtained BCN-HT100 possessed ultrathin nanosheet structure with high polymerization degree, large surface area and plenty of pores.
- Photocatalytic overall water splitting was achieved with the AQY reaching 5.8% at 380 nm and 4.9% at 405 nm.

GRAPHICAL ABSTRACT
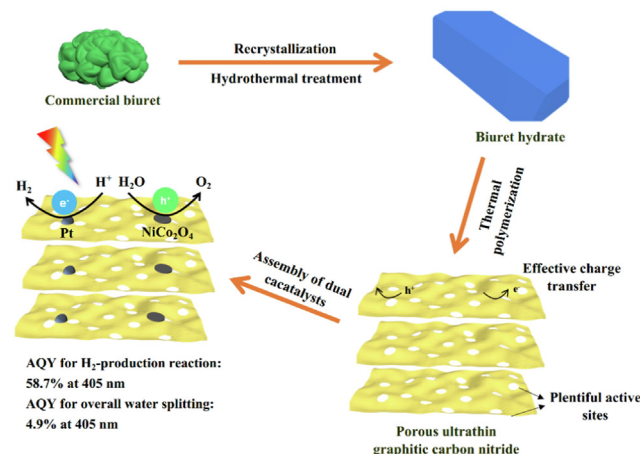
AQY for H2-production reaction: 58.7% at 405 nm
AQY for overall water splitting: 4.9% at 405 nm

ABSTRACT

Structure regulation (including electronic structure and morphology) for graphitic carbon nitride (g-C$_3$N$_4$) is an effective way to promote the photocatalytic activity. Herein, an ultrathin porous g-C$_3$N$_4$ (BCN-HT100) was synthesized by calcination of biuret hydrate. Hydrothermal treatment induced biuret recrystallization to form biuret hydrate precursor with regular morphology and large crystal size, thus promoting the polymerization of melem to form g-C$_3$N$_4$ network. Accordingly, BCN-HT100 possessed ultrathin nanosheet structure, higher polymerization degree, larger surface area and more pores than biuret-derived g-C$_3$N$_4$. BCN-HT100 behaved high-efficiency photocatalytic H$_2$-productin activity with an apparent quantum yield (AQY) of 58.7% at 405 nm due to the enhanced utilization efficiency for photo-generated charge carriers and abundant reactive sites. Furthermore, Pt-NiCo$_2$O$_4$ dual cocatalysts were employed on BCN-HT100 for achieving photocatalytic overall water splitting, and the AQY reached

* Corresponding author at: International Research Center for Renewable Energy (IRCRE), State Key Laboratory of Multiphase Flow in Power Engineering (MFPE), Xi'an Jiaotong University (XJTU), 28 West Xianning Road, Xi'an 710049, PR China.
E-mail address: jinwen_shi@mail.xjtu.edu.cn (J. Shi).

Solar energy
Solvothermal treatment

4.9% at 405 nm. This work provides a meaningful reference to designing g-C_3N_4 to achieve efficient solar energy conversion into hydrogen.

1. Introduction

Hydrogen production via solar-driven water splitting has been considered to be a promising strategy for cost-effective storage of solar energy [1,2]. This "solar-to-hydrogen" technology can date back to 1972 when Fujishima and Honda reported the discovery of photoelectrochemical water splitting on the titania electrode [3], and it subsequently draws extensive attention in view of the promising application in the important energy and environmental crisis. Development of available, visible-light-responsive and low-cost photocatalysts is the critical step for this photocatalysis technology to realize its practical application [4–6]. Graphitic carbon nitride (g-C_3N_4), which takes fascinating merits of low cost, proper electronic properties and good stability, has been widely investigated in solar-light-derived photocatalytic H_2 production [7–10]. However, developing high-efficiency g-C_3N_4 for photocatalytic H_2 production is still the main challenge because the small surface area and severe charge carriers recombination are the main obstacle. Precursor usually plays dominant role in determining the electronic and textural properties of g-C_3N_4 [11–14], investigation focused on precursor structure is always an effective approach to yield high-efficiency g-C_3N_4.

Precursor materials have significant effects on the properties of correspondingly derived g-C_3N_4. For the precursor material of a single substance, on the one hand, C, N and H elements from the precursor participate in the formation of g-C_3N_4, other additional leaving motifs (eg. S and O) contained in some precursors can promote the packing and connectivity of heptazine units, thereby facilitating the polymerization and condensation degree of g-C_3N_4 [15–17]. On the other hand, for the multicomponent precursor, the different molecules of components lead to different routes/processes for undergoing polymerization reaction at high temperature to form g-C_3N_4 networks [14,18,19]. Moreover, precursors' different components of elements and nitrogen content ultimately result in different proton concentration and structure defects of g-C_3N_4 [20–22], thus affecting the polymerization degree, ordering in long-range atomic arrangements and inter-layer stacking of conjugated aromatic systems. In addition, the particle size and morphology of the precursors also can affect the morphology, surface area and pore structure of g-C_3N_4 [23–25]. As a result, it can be found that the precursor material directly determines the crystal structure, electronic structure and micro-nano morphology of the corresponding derived g-C_3N_4, consequently manifested in the enhancement of solar-light-derived photocatalytic water splitting performance.

Structure and composition modification of the precursors make for obtaining high-efficiency g-C_3N_4, and one of the most commonly used modification strategies is solvothermal method [19,26–28]. According to the chemical and physical properties, precursors are treated in appropriate solvents with relatively high temperature and pressure, recrystallization occurs after solvothermal reaction, the crystallinity, morphology and even components for the precursors change, thus making an impact on the morphology, crystalline and electronic properties of the corresponding obtained g-C_3N_4. Mo et al. reported a strategy of treating melamine by hydrothermal reaction at 200 °C for different time [26]. Melamine converted into cyanuric acid partially, then melamine together with cyanuric acid formed supramolecular intermediate by self-assembly. This supramolecular intermediate-derived g-C_3N_4 nanotubes had lots of nitrogen defects and behaved much

improved photocatalytic H_2-production activity compared with the directly melamine-derived g-C_3N_4. In addition, Han et al. developed an antisolvent growth technique to synthesize size-reduced urea crystallizes from methanol-supersaturated solution [29], then defect-rich amorphous carbon nitride was obtained by pyrolysis of the modified urea and showed dramatically enhanced photocatalytic efficiency with respect to pristine urea-derived g-C_3N_4.

In our previous work, it has been proved that commercially purchased biuret-derived g-C_3N_4 behave high photocatalytic H_2-production activity [13]. In addition, commercially purchased biuret usually comprise biuret and biuret hydrate. Suitable solvothermal treatment for commercially purchased biuret could change the components and structure, which would greatly influence the polymerization degree and micro-nano structure of the correspondingly derived g-C_3N_4. Herein, the commercially purchased biuret was treated by hydrothermal and different solvothermal reactions for a certain time, then the recrystallized intermediate underwent pyrolysis to form g-C_3N_4 framework with polymerization degree and structure regulation. Moreover, systematic characterizations and analysis were carried out to demonstrate the changes in the composition and structure for the precursor before and after hydrothermal and solvothermal reaction, as well as investigate the electronic properties, degree of polymerization and textual structure for the derived g-C_3N_4.

2. Experimental section

2.1. Materials

All reagents were of analytical grade and were used without further purification, and the reagents were obtained from Sinopharm Chemical Reagent Co., Ltd except that $H_2PtCl_6·6H_2O$ was purchased from Alfa Aesar.

2.2. Preparation of samples

2.2.1. Solvothermal treatment of precursor

The commercially purchased biuret was abbreviated as BU. BU powder (2 g) was put into deionized water (20 mL) in a Teflon-lined autoclave (100 mL) under stirring. A dispersion was obtained. Then the autoclave was sealed and maintained at 100 °C for 12 h. After natural cooling, the product was alternately washed with deionized water 3 times and collected by centrifugation to remove the residues of reactants, followed by drying in vacuum at 50 °C overnight. The obtained precursor material was denoted as BU-HT100. Other precursor products (denoted as BU-HT80 and BU-HT120, respectively) were prepared by following the same procedure except for the different hydrothermal temperatures (80 °C and 100 °C, respectively). Other precursor products (denoted as BU-MeOH100, BU-EtOH100 and BU-DMF100, respectively) with different solvothermal solvents were also prepared by following the same procedure except that the solvents were adjusted as required (methanol (MeOH), ethanol (EtOH) and N,N-dimethylformamide (DMF), respectively).

2.2.2. Preparation of g-C_3N_4

BU-HT100 (1 g) powder was put into an alumina crucible with a cover, and then calcined at 550 °C (ramping rate, 5 °C min^{-1}) under Ar atmosphere for 4 h. After natural cooling, the final pro-

duct was collected and denoted as BCN-HT100. Other products (denoted as BCN, BCN-HT80, BCN-HT120, BCN-MeOH100, BCN-EtOH100 and BCN-DMF100, respectively) derived from different precursors (BU, BU-HT80, BU-HT120, BU-MeOH100, BU-EtOH100 and BU-DMF100, respectively) were prepared by following the same procedure.

2.2.3. Preparation of 3Pt/BCN-HT100/2NiCo₂O₄

3Pt/BCN-HT100/2NiCo$_2$O$_4$ was prepared according to the previous work with using BCN-HT100 as the photocatalyst [10].

2.3. Sample characterization

Powder X-ray diffraction (XRD) patterns were obtained from a PANalytical X'pert MPD diffractometer operated at 40 kV and 40 mA using Ni-filtered Cu Kα irradiation (λ = 1.5406 Å). Fourier transform infrared spectra (FTIR) were recorded by a Bruker Vertex 70 FTIR spectrophotometer with using the KBr pellet technique. Field-emission scanning electron microscopy (FESEM) images were observed on a JEOL JSM-7800F instrument. Thermogravimetric-differential scanning calorimetry (TG-DSC) curves were recorded by a thermal analyzer NETZSCH STA 449C, Germany) in the range from 40 to 600 °C. Electron paramagnetic resonance (EPR) experiments were performed on a Bruker EMX X-band spectrometer and microwave frequency = 9.40 GHz at room temperature. X-ray photoelectron spectroscopy (XPS) spectra were obtained on a Kratos Analytical Axis Ultra DLD instrument with a monochromatized Al Kα line source (150 W). All binding energies were referenced to the C 1s peak at 284.8 eV. Elemental compositions for g-C$_3$N$_4$ were obtained from an elemental analyzer (EA) of vaeeio MACRO cube. Synchrotron-based X-ray absorption near-edge structure (XANES) spectroscopy for C K-edge and N K-edge were obtained from BL20A, at the National Synchrotron Radiation Research Center, Taiwan. Transmission electron microscopy (TEM) images were obtained from an FEI Tecnai G^2 F30 S-Twin transmission electron microscope with an accelerating voltage of 300 kV. Atomic force microscopy (AFM) image was obtained from a NT-MDT Solver Next atomic force microscope. Surface area and porosity measurement was carried out by N$_2$ adsorption on a Micromeritics ASAP 2020 plus instrument using the Brunauer–Emmette–Teller (BET) method. UV–vis absorption spectra (UV–vis) were measured on a Agilent Cary 5000 instrument equipped with a diffuse-reflectance accessory and with BaSO$_4$ as the reference. Photoluminescence spectra (PL) analysis was carried out on a PTI QuantaMaster 40 steady-state/time-resolved fluorescence spectrophotometer equipped with an excitation wavelength of 337/460 nm at room temperature, N$_2$ was filled in the instrument when the test of time-resolved transient PL decay spectra.

Calculation method about transient PL decay kinetics was depicted as follows. In the present study, the emission signals were analyzed by the method of tri-exponential decay kinetics. The following equation was employed to calculate average lifetime τ_{avg}.

$$\tau_{avg} = \frac{\sum A_i \tau_i^2}{\sum A_i \tau_i}$$

2.4. Photocatalytic performance measurement

Photocatalytic H$_2$ production was performed in a sealed Pyrex glass cell (100 mL) with a side window for external light incidence under constant magnetic stirring. A Xe lamp (300 W) equipped with a UV-cutoff filter (λ > 400 nm) was used as the visible-light source. In the photocatalytic process, triethanolamine (TEOA), MeOH, formic acid or lactic acid functioned as sacrificial agent to consume photogenerated holes. In detail, photocatalyst (10 mg)

and aqueous solution (80 mL) (10 vol% TEOA, 20 vol% MeOH, 10 vol% formic acid and 10 vol% lactic acid, respectively) were mixed in the glass cell with stirring. Pt (3 wt%) as cocatalyst was photo-deposited in situ on photocatalyst from the precursor of H$_2$-PtCl$_6$·6H$_2$O. Before photocatalytic reaction, Ar was bubbled into the cell for 15 min to remove O$_2$. The evolved H$_2$ was analyzed on a North Point NP-GC-901A gas chromatograph (thermal conductivity detector (TCD), TDX-01 column, Ar as carrier gas) per 1 h.

Photocatalytic O$_2$ production reaction was performed in the same system, photocatalyst (50 mg), La$_2$O$_3$ (160 mg) and AgNO$_3$ (136 mg) were sequentially dispersed in deionized water (80 mL) with stirring, in which AgNO$_3$ and La$_2$O$_3$ were used as electron acceptor and pH buffer agent, respectively. Before photocatalytic reaction, the reactor was purged with Ar for 30 min to eliminate O$_2$.

Photocatalytic overall water splitting reaction was performed in the same system, 3Pt/BCN-HT100/2NiCo$_2$O$_4$ photocatalyst (50 mg) was dispersed into deionized water (80 mL) with stirring. Before photocatalytic reaction, the reactor was purged with Ar for 30 min to eliminate O$_2$.

The measurement of AQY was carried out under the irradiation of 300 W Xe lamp equipped with a band-pass filter (405, 425, 440, 480, 520 and 550 nm). For photocatalytic H$_2$ production reaction, photocatalyst (50 mg) was added into the reaction solution of 80 mL 10 vol% TEOA aqueous solution with 0.08 mol of K$_2$HPO$_4$. Pt (3 wt%) as cocatalyst was photodeposited in situ on photocatalyst from the precursor of H$_2$PtCl$_6$·6H$_2$O. For photocatalytic overall water splitting reaction, the AQY was measured in the same procedure, 3Pt/BCN-HT100/2NiCo$_2$O$_4$ photocatalyst (50 mg) was dispersed into pure water (80 mL) with stirring. The intensity of incident light was recorded by a spectroradiometer (Avantes AvaSpec-2048-USB2, Netherlands). The AQY value was obtained by the following equation:

$$AQY(\%) = \frac{\text{Number of reacted electrons}}{\text{Number of incident photons}} \times 100$$

$$= \frac{\text{Number of evolved H}_2 \text{ molecules} \times 2}{\text{Number of incident photons}} \times 100$$

2.5. Electrochemical measurement

(Photo)electrochemical measurement was carried out in a three-electrode chemical cell by using a CH Instruments CHI 760D scanning potentiostat. Pt foil and Ag/AgCl electrode were applied as the counter electrode and reference electrode, respectively, and N$_2$-saturated Na$_2$SO$_4$ aqueous solution (0.5 M) was employed as the electrolyte. To prepare the working electrodes for electrochemical measurements, the as-prepared photocatalyst (1 mg) was first ultrasonically dispersed in the mixture of deionized water (250 μL), ethanol (250 μL), and Nafion solution (10 μL, 10 wt%) for 1 h to form a homogeneous suspension, and then the above suspension (10 μL) was transferred onto a glassy carbon rotating disk electrode (RDE, CHI 104, 3 mm of diameter,) via a controlled drop casting approach. After the natural drying under ambient temperature, the resulting electrode was obtained to serve as the working electrode. Linear sweep voltammetry (LSV) curves were conducted at a scan rate of 10 mV/s. The measured potentials vs. Ag/AgCl were converted to reversible hydrogen electrode (RHE) scale via the Nernst equation.

3. Results and discussion

3.1. Structures and morphologies for BU and BU-HT100

Figs. S1 and 1a show the XRD patterns for all the precursors after hydrothermal and different solvothermal treatments. The rel-

atively high temperature and pressure in reaction usually can change the crystal structure and morphology of the material, resulting in phase transformation. It can be observed BU contained two components of biuret and biuret hydrate, BU-EtOH100 and BU-DMF100 were mainly composed of biuret, while BU-MeOH100 and BU-HT100 dominantly consisted of biuret hydrate. In addition, BU-HT100 showed pretty high peak intensities, indicating the biuret hydrate obtained by hydrothermal treatment could possess good crystallinity. The hydrothermal reaction made BU purified and recrystallized, and biuret converted into biuret hydrate which was precipitated in an aqueous environment after temperature went down. Fig. 1b shows the FTIR of BU and BU-HT100 samples. Both samples showed similar spectra which could belong to typical peaks of the structural feature for biuret, the peak at 3100–3500, 1600–1700, 1000–1600 and 600–800 cm^{-1} were

assigned to the stretching vibrational absorptions of N—H bonds (as well as an overlapping band of –OH stretching), stretching vibrations of C—O, stretching vibrations of C—N and the bending vibrations of N—H, respectively [30,31]. But the wavenumber ranges attributed to the C—N stretching peaks for BU-HT100 were blue-shifted compared with those of BU, the shifts were speculated to be caused by the more combination of crystal water. In addition, Fig. 1c and d show the SEM images of BU. BU had cumulated irregular block structure with irregular boundary shape, and the surface was rough and the size was about tens to hundred micrometers. BU-HT100 mainly possessed regular shapes with rectangular plate-like structure, the surface was relatively smooth and the sizes were generally larger than one hundred micrometers (Fig. 1e and f). The conversion from BU into BU-HT100 could be regarded as a recrystallization process, on the one hand, biuret
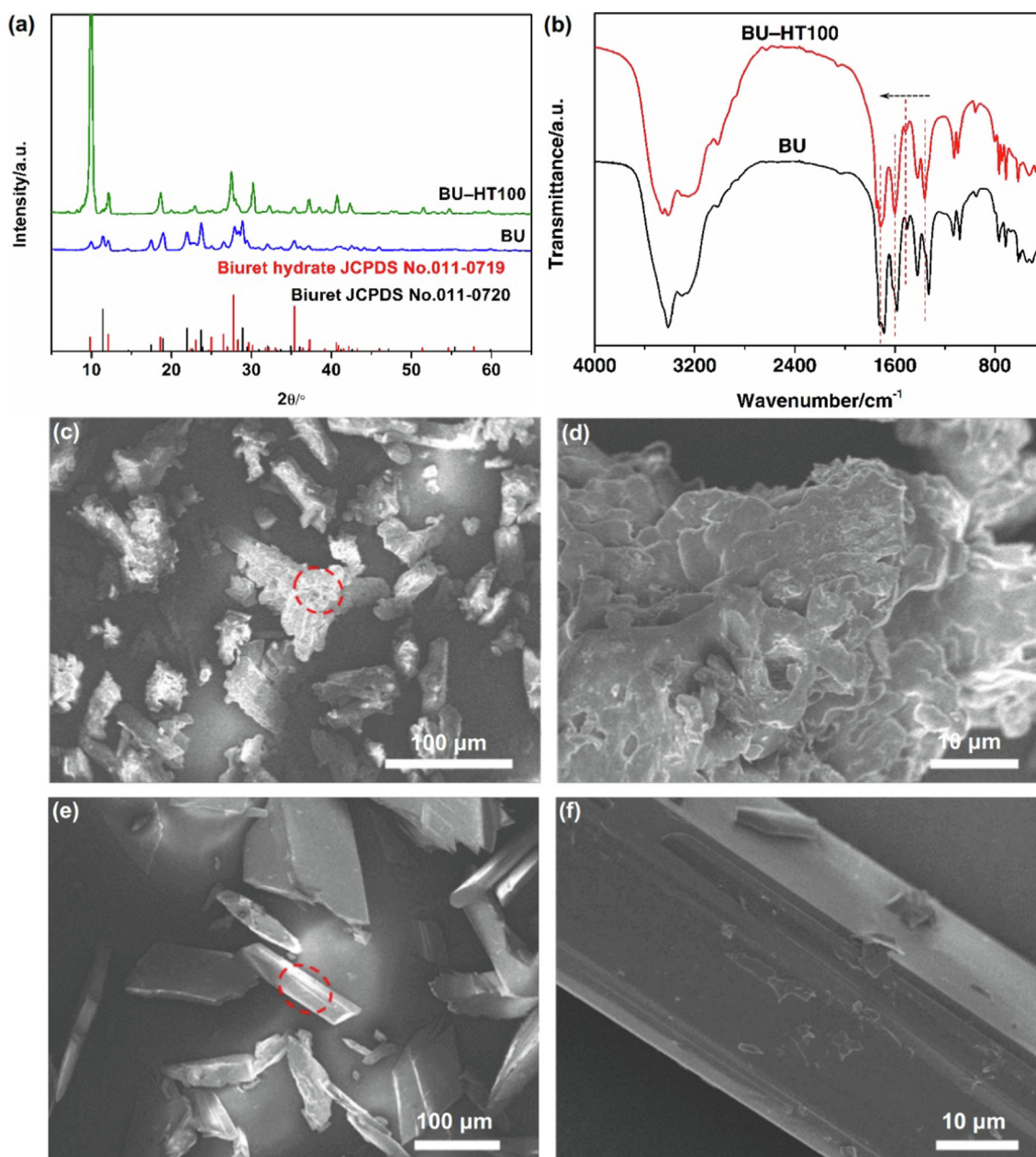

Fig. 1. (a) XRD patterns and (b) FTIR spectra for BU and BU-HT100. (c-f) SEM images for (c, d) BU and (e, f) BU-HT100. Scale bar: (c, e) 100 μm, (d, f) 10 μm. (d and f) were the magnified results for the red circles in (c and e), respectively. (For interpretation of the references to colour in this figure legend, the reader is referred to the web version of this article.)

was converted to biuret hydrate, on the other hand, crystal particles grew into regular geometric structures. Fig. S2 presents the SEM images for BU-HT80 and BU-HT120. As compared to BU-HT100, BU-HT80 showed the aggregated plate-like structure with rugged surface, and BU-HT120 showed plate-like structure with regular surface. However, the three kinds of precursors all not had uniform particle sizes. Fig. S3 presents the SEM images for BU-MeOH100, BU-EtOH100 and BU-DMF100, and the three kinds of precursors did not have regular geometric structures. BU-HT100 and BU-MeOH100 had larger particle sizes than BU-EtOH100, BU-DMF100 and BU. According to the XRD results, BU-HT100 and BU-MeOH100 dominantly consisted of biuret hydrate, while BU-EtOH100 and BU-DMF100 were mainly composed of biuret. It indicated that biuret could be converted to biuret hydrate in hydrothermal and MeOH-based solvothermal treatments via recrystallization process. However, only hydrothermal treatment could lead to regular geometric structure for biuret hydrate precursor.

3.2. Structures and chemical states for BCN and BCN-HT100

BU and BU-HT100 were subsequently employed as precursors to prepare g-C_3N_4 via thermal polymerization under Ar atmosphere, and Fig. 2a presents the schematic illustration about the preparation process of BCN-HT100. For the TG-DSC analysis, as shown in Fig. 2b, there had five stages of phase transition and mass loss in the thermal polymerization process: water expulsion, decomposition, polymerizing to form melamine, melamine polymerization to form melem, and melem polymerization to yield g-C_3N_4 [29,32,33]. As compared to BU, the TG-DSC analysis of BU-HT100 showed the increased temperatures in water expulsion and melem formation, indicating the high content of biuret
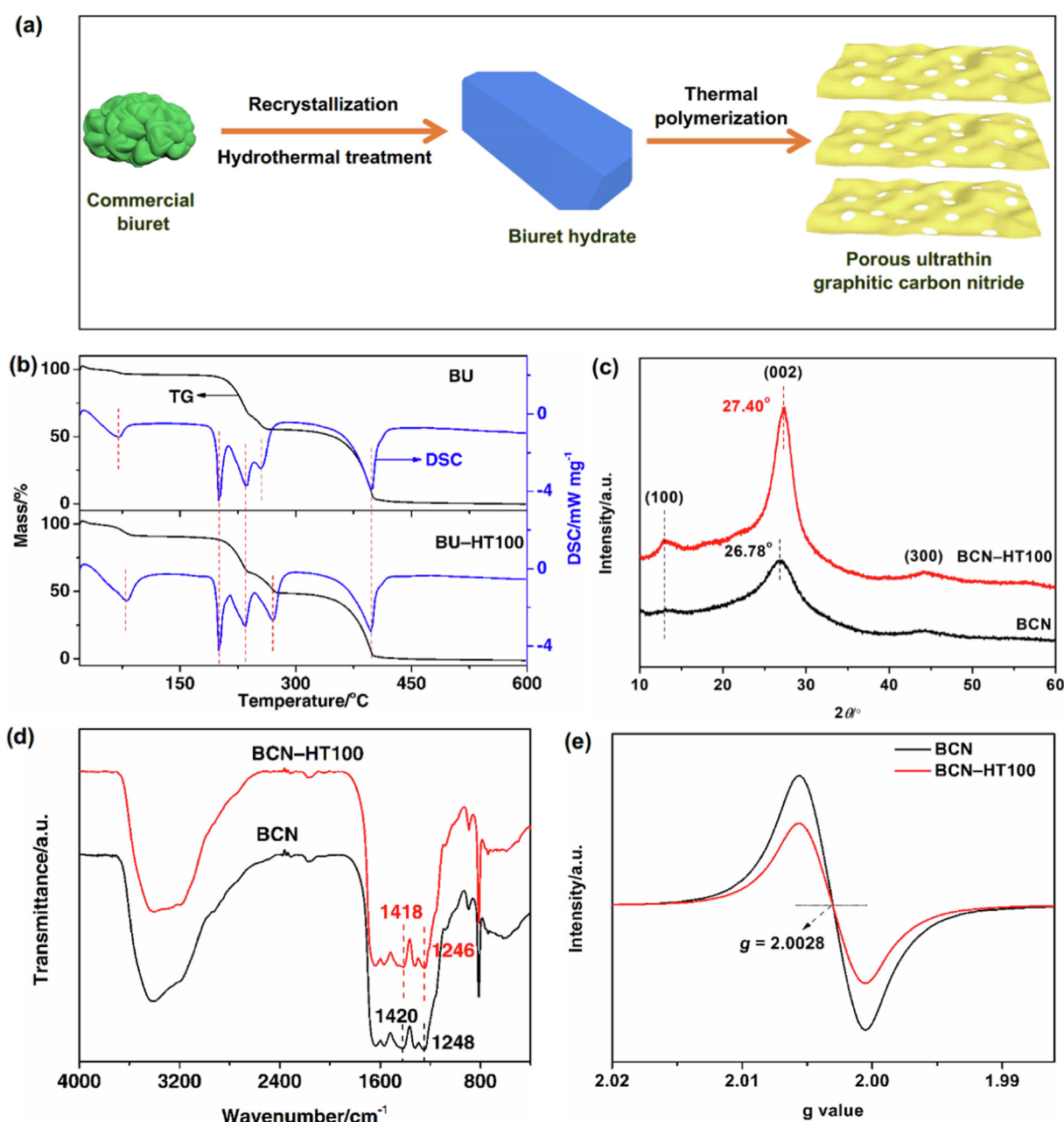

Fig. 2. (a) Schematic illustration about the preparation process of BCN-HT100. (b) TG-DSC curves, (c) XRD patterns, (d) FTIR spectra and (e) EPR spectra for BCN and BCN-HT100.

hydrate and large precursor size resulted in higher temperature of thermal polycondensation. It could be inferred that the increased temperature of BU-HT100 could promote the polymerization of melem to form of g-C$_3$N$_4$ framework, which had a vital impact on the structural properties and performance of the derived g-C$_3$N$_4$. Figs. S4 and 2b show the XRD patterns for all the g-C$_3$N$_4$ samples. BCN had disordered nitrogen-defect-rich carbon nitride structure as our previous report [13]. BCN-MeOH100, BCN-EtOH100 and BCN-DMF100 had similar XRD patterns to BCN. BCN-HT100 had stronger intensity for (1 0 0) peak than BCN, indicating BCN-HT100 contained more orderly arrangement tri-s-triazine (heptazine) structure. Furthermore, the (0 0 2) peak of BCN-HT100 was much stronger and located at a higher angle (27.40°) as compared to that of BCN (26.78°), implying that BCN-HT100 possessed higher degree of polymerization and tighter packing of nanosheets than BCN [15,34]. Fig. 2c presents the FTIR spectra of BCN and BCN-HT100. Both samples showed similar spectra and the typical characteristic peaks could belong to the structural feature of g-C$_3$N$_4$, while there existed some difference that the two peaks which were attributed to bridging C-NH-C units of heptazine for BCN-HT100 located at relatively lower wavenumbers than those for BCN. Moreover, the EPR analysis showed BCN-HT100 had weaker signal than BCN (Fig. 2d), which indicated BCN-HT100 had less lone electron pairs than BCN [15,35]. The FTIR and EPR results suggested BCN-HT100 had less N defects than BCN. As a result, it can be concluded that the regular shapes with rectangular plate-like structure and large crystal particle size of BU-HT100 made accordingly derived BCN-HT100 had more ordered struc-tures and higher degree of polymerization with less N defects as compared to BU-derived BCN.

Fig. 3a and b show the C 1s and N 1s XPS spectra of BCN and BCN-HT100, respectively. Both samples generally presented similar characteristic peaks indexed to g-C$_3$N$_4$. For the C 1s spectra (Fig. 3a), the peaks of BCN-HT100 could be fitted and indexed to standard carbon C=C (284.8 eV), sp^2-hybridized C in C−NH & C−NH$_2$ (286.2 eV), and sp^2 C linked to N in N−C=N (288.3 eV), respectively [36–38]. The peak indexed to N−C=N for BCN-HT100 centered at lower binding energy than that for BCN (288.6 eV), indicating BCN-HT100 had less N defects located in heptazine units. Furthermore, BCN-HT100 showed pretty larger peak-area ratio for N−C=N to C−NH & C−NH$_2$ (Table S1), indicat-ing a relatively more quantity of C 2p orbital in BCN-HT100, this result indicated BCN-HT100 had much more ordered structures than BCN [15,39]. For the N 1s spectra (Fig. 3b), the peaks of of BCN-HT100 could be fitted and indexed to the sp^2-nitrogen in N−C=N (N$_{2C}$) (398.5 eV), tertiary nitrogen in N−(C)$_3$ (N$_{3C}$) groups (399.3 eV), nitrogen in heterocycles N─H (400.8 eV) and π-excitation (404.4 eV), respectively [36–38]. N$_{2C}$ and N$_{3C}$ participate in the construction of the basic heptazine heterocyclic ring (C$_6$N$_7$) substructure for g-C$_3$N$_4$. The peak-area ratio of sp^2 C−N=C bonds to the sum of sp^3 N−(C)$_3$ and N─H bonds for BCN-HT100 (1.5) was larger than that of BCN (1.4) (Table S1), indicating that BCN-HT100 had higher degree of polymerization than BCN [15,39]. In addition, EA results showed the atomic ratio of carbon to nitrogen for BCN-HT100 (0.70) was also larger than that for BCN (0.69) (Table S2), and BCN-HT100 have less content of H element than BCN, both further demonstrating the higher polymerization degree
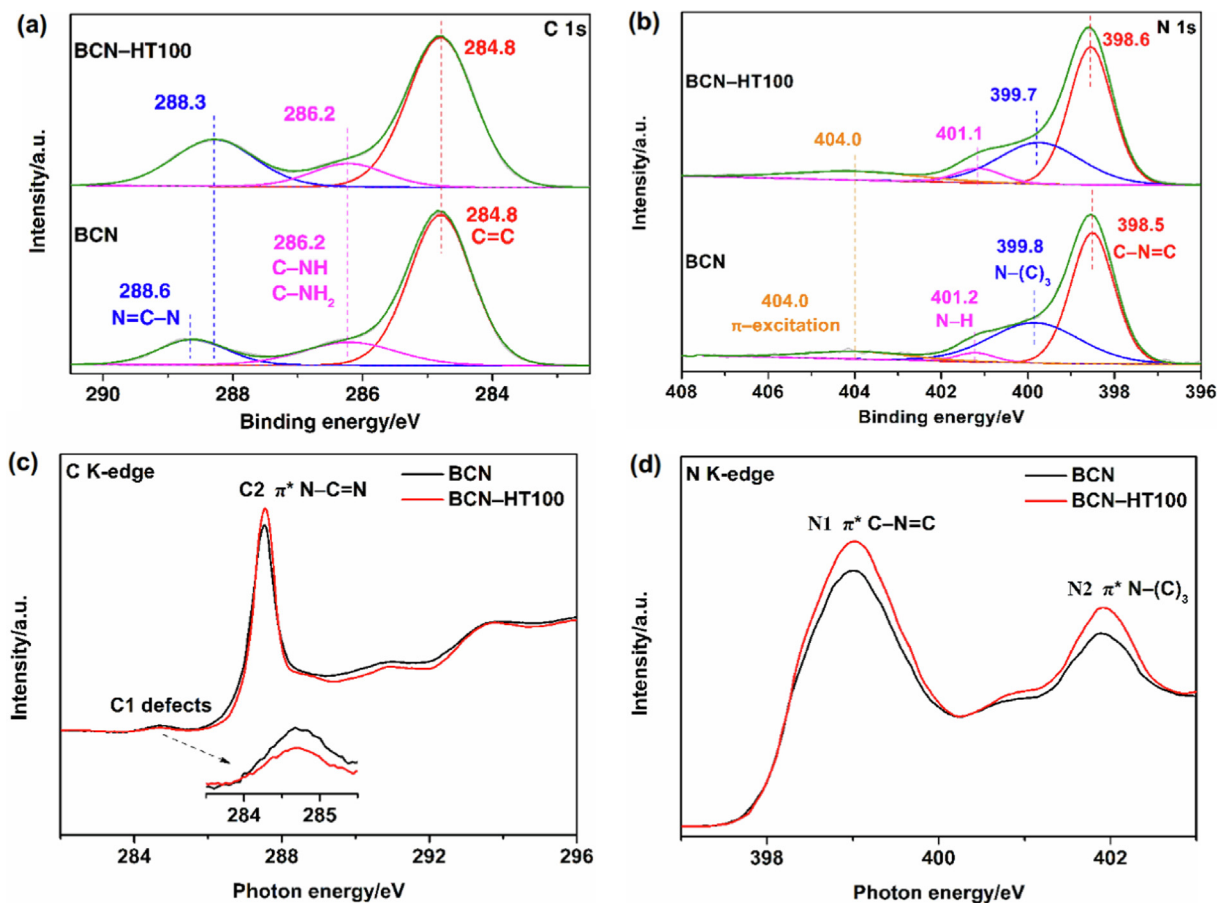

Fig. 3. (a, b) High-resolution XPS spectra of (a) C 1s and (b) N 1s, and (c, d) K-edge XANES spectra of (c) C and (d) N for BCN and BCN-HT100.

for BCN-HT100 [40,41]. Fig. 3c and d show the XANES spectroscopies of BCN and BCN-HT100. For the C K-edge XANES spectra (Fig. 3c), BCN-HT100 had weaker peak intensity of peak C1 and stronger peak intensity of C2 than BCN, indicating low concentration of carbon defects and more ordered structures in BCN-HT100 [13,42]. For the N K-edge XANES spectra (Fig. 3d), BCN-HT100 showed stronger peak intensities for both N1 and N2 peaks than BCN, implying BCN-HT100 contained more unsaturated states of N 2p orbitals. In addition, BCN-HT100 had larger N1/N2 peak intensity ratio than BCN (Table S3), indicating BCN-HT100 possessed higher polymerization degree and contained less nitrogen defects [42,43].

3.3. Micro-nano structures and textual properties for BCN and BCN-HT100

The micro-nano structures for BCN and BCN-HT100 were investigated by SEM, TEM, AFM and BET analysis. As shown in Fig. 4a and Fig. S5a, BCN possessed curly and chipping like structure without aggregation. The low-magnification TEM images (Fig. 4d and

Fig. S5c) revealed that BCN appeared as twisted thin layers. BCN-HT100 showed obviously porous structure with lots of pores (Fig. 4b and Fig. S5b), and TEM images showed BCN-HT100 appeared as a thinner layer structure with large "broken" holes, which looked like wet "broken" paper with holes (Fig. 4e and Fig. S5d). In addition, Fig. 4c shows the AFM diagram of BCN-HT100. The thickness of BCN-HT100 sheet was about 4 nm. Fig. S6 shows the SEM images for BCN-HT80 and BCN-HT120, both samples showed similar aggregated bulk structure. The results indicated that 100 °C was the proper hydrothermal temperature to treat biuret and thus obtained ultrathin porous g-C$_3$N$_4$ (BCN-HT100). Fig. S7 presents the SEM images for BCN-MeOH100, BCN-EtOH100 and BCN-DMF100. BCN-MeOH100 and BCN-DMF100 showed the similar structure of aggregated sheets. BCN-EtOH100 showed thin layer structure with lots of small pores. The morphologies for the three kinds of g-C$_3$N$_4$ were quite different from BCN-HT100, indicating that only hydrothermal treatment could result in thin and porous layer structure for g-C$_3$N$_4$. Fig. 4f shows the N$_2$ absorption–desorption isotherms for BCN and BCN-HT100. Both samples exhibited the type IV isotherms and had high
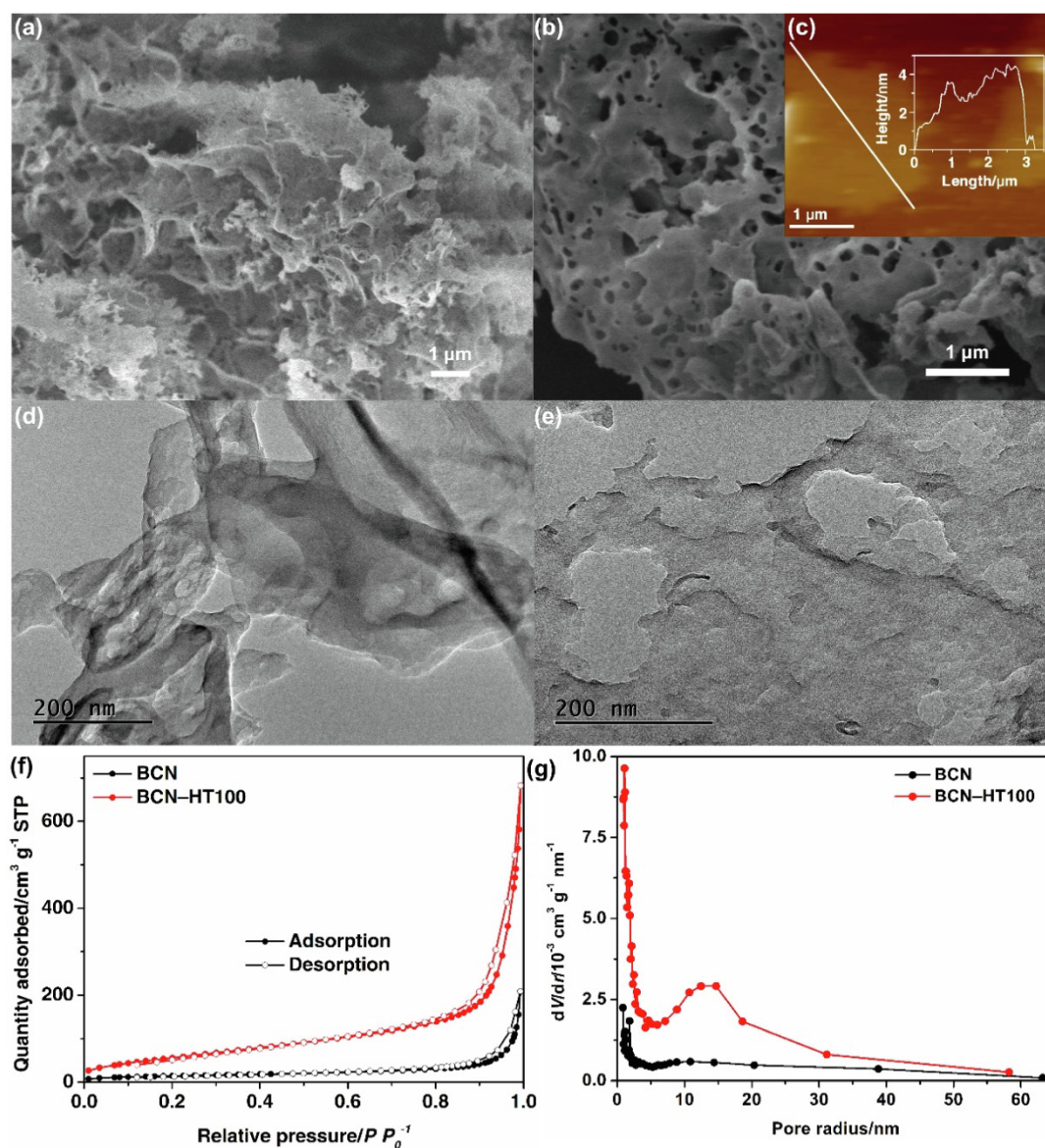

Fig. 4. (a, b) SEM images for (a) BCN and (b) BCN-HT100. (c) AFM image for BCN-HT100 (inset: height profile along the line in (c) of BCN-HT100). (d, e) TEM images for (d) BCN and (e) BCN-HT100. (f) N$_2$ adsorption–desorption isotherms and (g) derived pore-size distributions for BCN and BCN-HT100. Scale bar: (a-c) 1 μm, (d, e) 200 m.

adsorption capacities in $P/P_0 > 0.8$, indicating that there existed plenty of macropores and mesopores [44]. BCN-HT100 possessed a larger surface area (220.2 m² g⁻¹) as compared to BCN (51.5 m² g⁻¹), and BCN-HT100 had a larger pore volume (1.1 cm³ g⁻¹) but smaller pore size (8.2 nm) than BCN (pore volume: 0.3 cm³ g⁻¹ and pore size: 11.0 nm) (Table S4), implying BCN-HT100 had more pore structures than BCN. The pore-size distribution analysis (Fig. 4g) also showed BCN-HT100 had much more pores. The outstandingly large surface area and plentiful pores for BCN-HT100 could generate plenty of active sites and facilitate contact with the reaction substrate, leading to high photocatalytic performance.

3.4. Optical properties, photoexcitation processes and photo-generated charge carriers dynamics for BCN and BCN-HT100

Fig. S8a shows the UV–vis absorption spectra for BCN and BCN-HT100. BCN-HT100 showed a blueshift in the absorption edge compared with BCN, which was attributed to the quantum confinement effect caused by the reduced thickness of nanosheets [45]. In addition, BCN-HT100 showed weaker adsorption intensity in the spectral tail (600–800 nm) than BCN, mainly because of the relatively low content of nitrogen defects in BCN-HT100 [15]. Based on the Kubelka–Munk method, the bandgaps of BCN and BCN-HT100 were recorded as 2.45 and 2.57 eV, respectively (Fig. S8b). The valence band (VB) XPS spectra showed BCN-HT100 had a value of 0.01 eV positive than BCN for the valence band maximum (VBM) (Fig. S8c). According to our previous work, it could be inferred the VBM and conduction band minimum (CBM)

positions for BCN-HT100 were 1.39 and −1.18 V vs. RHE (Fig. S8d), respectively, demonstrating that BCN-HT100 had stronger driving force for O₂ and H₂ evolution. To reveal the structure benefits for photo-excited electron transition in photocatalytic process, the C K-edge and N K-edge XANES spectra were conducted under illumination and in the dark. As shown in Fig. 5a and b, it explored the photo-excited electron transition from the lone pair states (i.e., occupied states) to the π* states (i.e., unoccupied states) [13,43]. BCN and BCN-HT100 both showed higher intensities under light irradiation than those under dark conditions. Fig. 5a showed the irradiation-dark intensity variations of C K-edge XANES spectra for BCN-HT100 was much more obvious than that for BCN, indicating there generated plenty of unoccupied states on the conduction band of BCN-HT100 [13,42]. While Fig. 5b showed the irradiation-dark intensity variations of N K-edge XANES spectra for BCN-HT100 was smaller than those for BCN, which should be attributed to the low nitrogen defects content [42]. As a result, these differences indicated that BCN-HT100 structure was conducive to more effective electron excitation from the occupied state of the valence band to the unoccupied state of the conduction band. The steady-state PL spectra analysis presented that BCN-HT100 showed weaker intensity than BCN (Fig. 5c), revealing the efficient inhibition for the recombination of photo-generated charge carriers [10,46,47]. In addition, the transient PL decay spectra were also investigated to further reveal the transfer dynamics of charge carriers (Fig. 5d). The average lifetime of the carrier (τ_{avg}) for BCN-HT100 was determined to be 3.72 ns, which was smaller than that for BCN, implying that there existed additional nonradiative decay channels in BCN-HT100 for promoting the electron transfer [36].
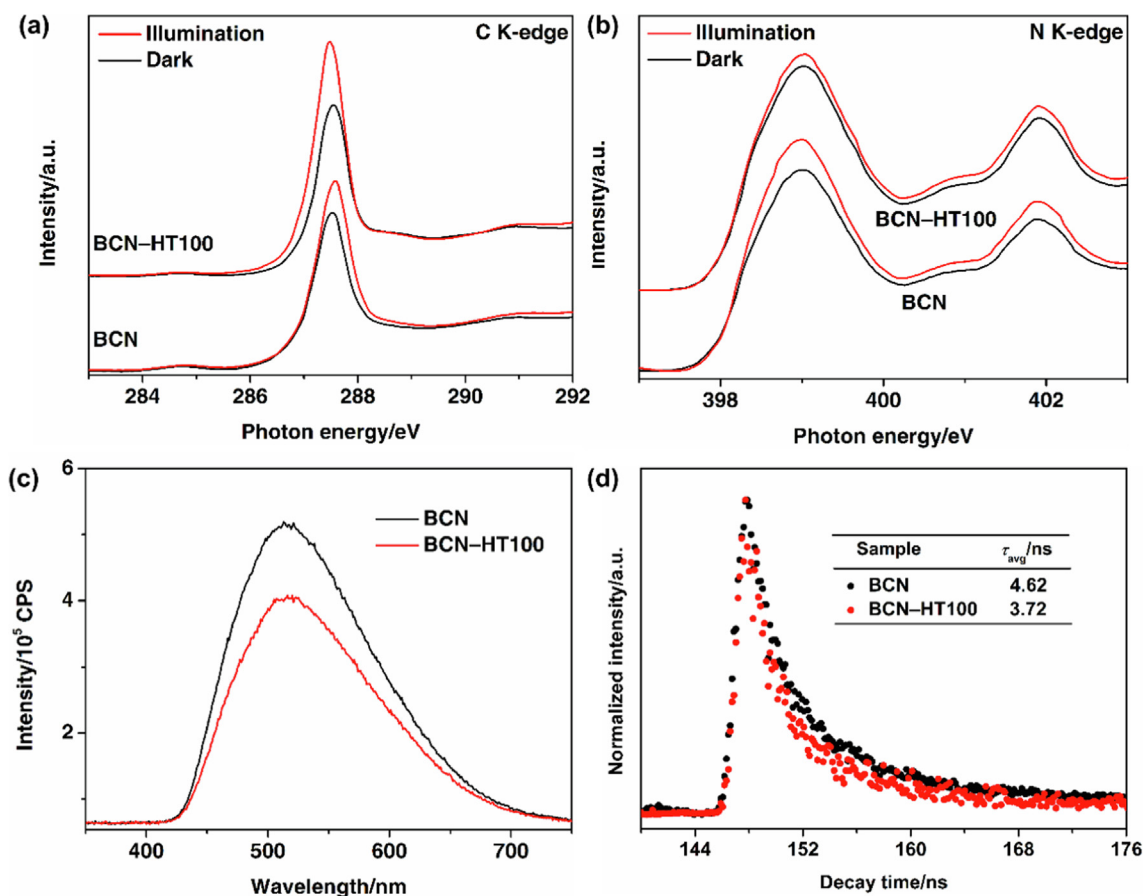

Fig. 5. (a, b) K-edge XANES spectra of (a) C and (b) N with "Illumination" or in "Dark" for BCN and BCN-HT100. (c) Steady state PL spectra and (d) transient PL spectra for BCN and BCN-HT100 at room temperature.

These enhanced carrier dynamics were mainly ascribed to the high polymerization degree and ultrathin nanosheets structure.

3.5. Photocatalytic performance for photocatalysts

Fig. S9 shows the photocatalytic H_2-production activities for BCN, BCN-HT80, BCN-HT100 and BCN-HT120 by using TEOA as sacrificial agent under visible-light irradiation. BCN-HT100 showed the highest photocatalytic H_2-production rate (21252 $\mu mol\ h^{-1}\ g_{cat}^{-1}$), which was about 2.4 times of BCN (8946 $\mu mol\ h^{-1}\ g_{cat}^{-1}$). In Fig. S10, it demonstrated that hydrothermal treatment of biuret could be the optimizing strategy to obtained high-efficiency graphitic carbon nitride because BCN-HT100 behaved the highest photocatalytic H_2-production activity. What's more, the photocatalytic H_2-production

performance for BCN-HT100 was also investigated in different sacrificial agent systems. In Fig. 6a, by adding K_2HPO_4 into TEOA-based photocatalytic system (mimicking natural photosynthesis [48]), the photocatalytic H_2-production activity of BCN-HT100 was promoted into a much high value (40457 $\mu mol\ h^{-1}\ g_{cat}^{-1}$). When using formic acid as sacrificial agent, the photocatalytic H_2-production rate for BCN-HT100 could be achieved the highest value (49178 $\mu mol\ h^{-1}\ g_{cat}^{-1}$). Fig. 6b shows the wavelength-determined AQYs for BCN-HT100 in (TEOA + K_2HPO_4)-based photocatalytic H_2-production system, the AQY reached 58.7% at 405 nm. Fig. S11 shows the wavelength-determined AQYs for BCN-HT100 in formic acid-based photocatalytic H_2-production system, the AQY achieved 64.2% at 405 nm. In addition, Table S5 summarized a comparison of photocatalytic H_2-production activities for BCN-HT100 and other representative gra-
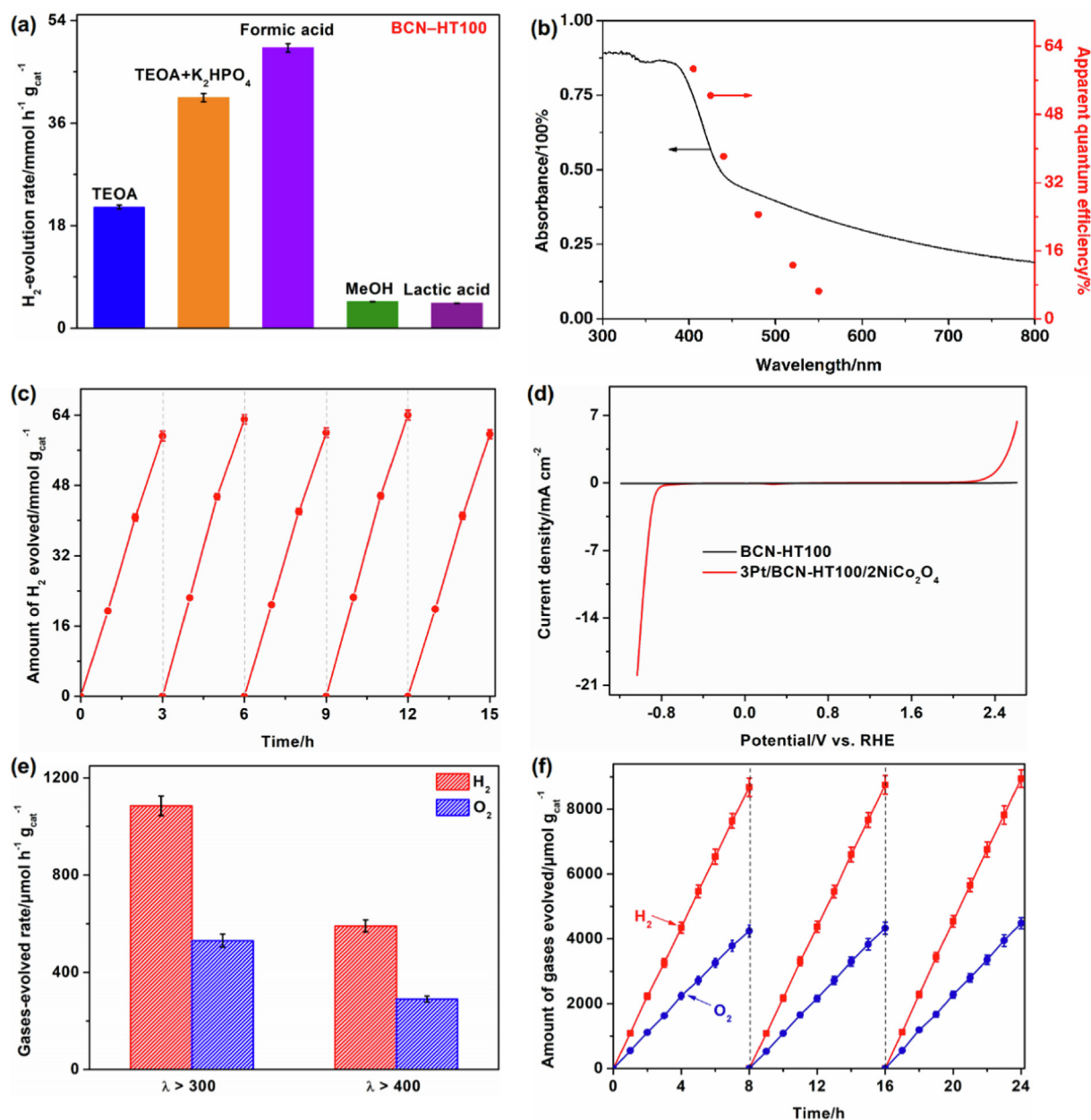

Fig. 6. (a) Photocatalytic H_2-production activities for BCN-HT100 using different sacrificial agents under visible-light irradiation (n = 3; mean ± SD) (n: the number of repeat experiments; SD: standard deviation). (b) Wavelength-determined AQYs for BCN-HT100 in (TEOA + K_2HPO_4)-based photocatalytic H_2-production system (The pH value for photocatalytic solution decreased a few from 10.9 to 10.4 after adding K_2HPO_4.). (c) Photocatalytic H_2-production stability test for BCN-HT100 under visible-light irradiation (n = 3; mean ± SD). (d) LSV curves for BCN-HT100 and 3Pt/BCN-HT100/2NiCo$_2$O$_4$ (electrolyte: 0.5 M Na_2SO_4). (e) Photocatalytic activities for overall water splitting on 3Pt/BCN-HT100/2NiCo$_2$O$_4$ under full-arc and visible-light irradiation (λ > 400 nm) (n = 3; mean ± SD). (f) Time courses of H_2 and O_2 production for photocatalytic overall water splitting under full-arc irradiation over 3Pt/BCN-HT100/2NiCo$_2$O$_4$ (n = 3; mean ± SD).
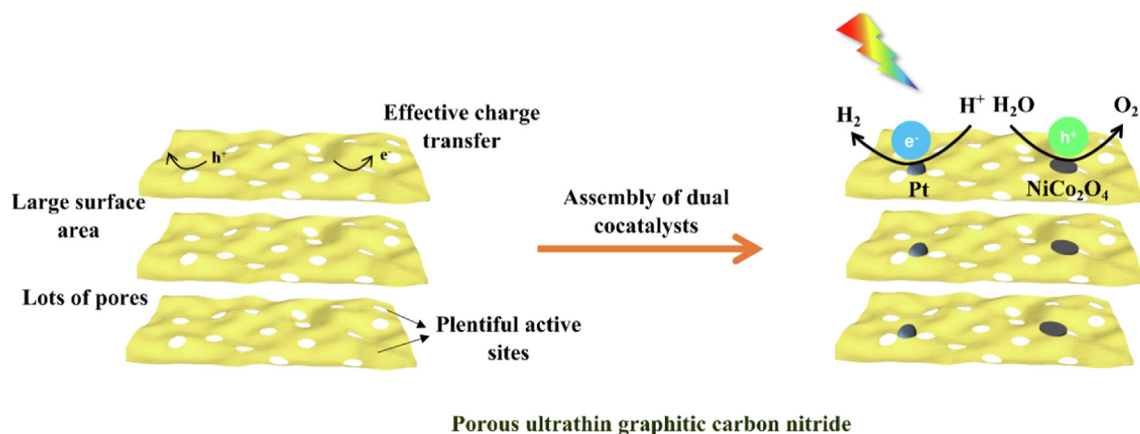
Fig. 7. Schematic mechanism of BCN-HT100 for photocatalytic H_2 and O_2 production.

phitic carbon nitrides. The AQY values for BCN-HT100 stood in the leading level for various carbon nitrides photocatalysts. Fig. 6c presents the cyclic test of photocatalytic H_2 production, little decay was observed for BCN-HT100 in five photocatalytic H_2-production cyclic tests (15 h). Furthermore, as shown in Fig. S12, XRD and FTIR measurements were employed to characterize the recovered photocatalyst (BCN-HT100-R) after photocatalytic $7H_2$-production reaction. For the XRD patterns, the peak intensity for BCN-HT100-R was almost no changed as compared to that for BCN-HT100, indicating the polymerization degree for BCN-HT100 was not changed during the photocatalytic process. While the (0 0 2) peak of BCN-HT100 shifted to a higher angle ($27.58°$) as compared to that of BCN ($27.40°$), implying that BCN-HT100 had a reunion of layers during the photocatalytic process. For the FTIR spectra, there was little difference between BCN-HT100-R and BCN-HT100, indicating the basic structure of BCN-HT100 was unchanged during the photocatalytic H_2 production. All the above results demonstrated that BCN-HT100 had good stability for the photocatalytic H_2 production. In addition, photocatalytic O_2-production performance for BCN and BCN-HT100 was measured by using $AgNO_3$ as the electron scavenger (Fig. S13). BCN-HT100 showed the photocatalytic O_2-production rate of 816 μmol h^{-1} g_{cat}^{-1}, which was about 2.4 times of BCN (311 μmol h^{-1} g_{cat}^{-1}). As a consequence, it could be inferred that BCN-HT100 had good potential to achieve photocatalytic overall water splitting due to its excellent photocatalytic H_2 and O_2 production performance. Pt-$NiCo_2O_4$ couple cocatalysts have been proved as an excellent alternative to promote photocatalytic overall water splitting for g-C_3N_4 [10]. Herein, Pt-$NiCo_2O_4$ were also applied on BCN-HT100, and Fig. 6d shows the linear sweep voltammetry (LSV) curves of BCN-HT100 and 3Pt/BCN-HT100/2$NiCo_2O_4$ for overall water splitting. It could be observed that 3Pt/BCN-HT100/2$NiCo_2O_4$ had significantly improved onset potentials for both H_2-evolution and O_2-production reaction, as well as enhanced cathode and anode current densities, indicating that dual Pt-$NiCo_2O_4$ cocatalysts could greatly accelerate photocatalytic overall water splitting for BCN-HT100. As expected, 3Pt/BCN-HT100/2$NiCo_2O_4$ showed simultaneously photocatalytic H_2 and O_2 production with a stoichiometric rate ratio of about 2: 1 under full-arc (1085 and 530 μmol h^{-1} g_{cat}^{-1}) and visible-light (590 and 290 μmol h^{-1} g_{cat}^{-1}) irradiation (Fig. 6e). The AQYs of 3Pt/BCN-HT100/2$NiCo_2O_4$ were determined to be 5.8% at 380 nm and 4.9% at 405 nm. Table S6 summarized a comparison of photocatalytic overall water splitting activities for BCN-HT100 and other graphitic carbon nitrides. BCN-HT100 presented good photocatalytic performance during various carbon nitrides photocatalysts. Fig. 6f shows the cyclic test of photocatalytic overall water splitting for 3Pt/BCN-HT100/2$NiCo_2O_4$, it also proved the good photocatalytic stability.

In summary, BCN-HT100 derived from BU-HT100 possessed higher polymerization degree, thinner nanosheet structure, larger surface area and lots of pores as compared to BCN derived from BU. Therefore, higher polymerization degree resulted in enhanced utilization of photo-generated charge carries; thinner nanosheet structure, larger surface area and lots of pores generated plenty of active sites. Fig. 7 shows the schematic mechanism of BCN-HT100 for photocatalytic H_2 and O_2 production. These advantages made synergistic effect to strongly support BCN-HT100 for achieving efficient photocatalytic activity. In addition, the CBM and VBM positions for BCN-HT100 were proper sufficiently to realize photocatalytic overall water splitting, suitable dual Pt-$NiCo_2O_4$ cocatalysts could promote the photocatalytic H_2 and O_2 production simultaneously.

4. Conclusions

Developing high-efficiency g-C_3N_4 photocatalyst is the key for realizing the application of photocatalytic H_2 production technology [9,13]. The small surface area and terrible charge carriers recombination severely limit the photocatalytic activity of g-C_3N_4 [19,38,47]. Although various strategies have been devoted to resolve the problem, such as exfoliation [42,49], nanostructure design [23,50], defect engineering [26], the efficiency requirement has not been achieved and more efforts should be taken to further improve the photocatalytic activity. Herein, an utrathin porous g-C_3N_4 (BCN-HT100) was prepared by calcination of biuret hydrate which was obtained from hydrothermal treatment on biuret and had regular morphology and large crystal size. The structure traits of biuret hydrate promoted the polymerization of melem to construct g-C_3N_4 framework with high polymerization degree and ultrathin porous nanosheet structure, leading to facilitated utilization of photo-generated charge carries and abundant reactive site. As a result, BCN-HT100 behaved high-efficiency photocatalytic H_2-evolution activity and the AQY reached 58.7% at 405 nm, which stood in the leading level for various carbon nitrides photocatalysts. Furthermore, with assembling Pt-$NiCo_2O_4$ dual cocatalysts on BCN-HT100, photocatalytic overall water splitting was achieved with an AQY of 4.9% at 405 nm. This work provides a strategy reference for designing g-C_3N_4 to achieve high-efficiency solar-to-hydrogen conversion via photocatalytic water splitting.

CRediT authorship contribution statement

Cheng Cheng: Conceptualization, Methodology, Validation, Writing – original draft, Investigation, Funding acquisition. **Jinwen**

Shi: Writing – review & editing, Supervision, Project administration, Resources, Funding acquisition. **Liuhao Mao:** Methodology, Formal analysis, Investigation. **Chung-Li Dong:** Methodology, Formal analysis. **Yu-Cheng Huang:** Methodology, Formal analysis. **Shichao Zong:** Methodology, Formal analysis. **Jiamei Liu:** Methodology, Formal analysis. **Shaohua Shen:** Writing – review & editing, Investigation. **Liejin Guo:** Supervision, Project administration, Resources, Funding acquisition.

Data availability

Data will be made available on request.

Declaration of Competing Interest

The authors declare that they have no known competing financial interests or personal relationships that could have appeared to influence the work reported in this paper.

Acknowledgements

Appendix A. Supplementary material

Supplementary data to this article can be found online at https://doi.org/10.1016/j.jcis.2023.01.098.

References

[1] T. Hisatomi, K. Domen, Reaction systems for solar hydrogen production via water splitting with particulate semiconductor photocatalysts, Nat. Catal. 2 (2019) 387–399.

[2] Y. Yang, C. Zhou, W. Wang, W. Xiong, G. Zeng, D. Huang, C. Zhang, B. Song, W. Xue, X. Li, Z. Wang, D. He, H. Luo, Z. Ouyang, Recent advances in application of transition metal phosphides for photocatalytic hydrogen production, Chem. Eng. J. 405 (2021) 126547.

[3] A. Fujishima, K. Honda, Electrochemical photolysis of water at a semiconductor electrode, Nature 238 (1972) 37–38.

[4] Z. Zhou, Y. Zhang, Y. Shen, S. Liu, Y. Zhang, Molecular engineering of polymeric carbon nitride: advancing applications from photocatalysis to biosensing and more, Chem. Soc. Rev. 47 (2018) 2298–2321.

[5] Y. Wang, H. Suzuki, J. Xie, O. Tomita, D.J. Martin, M. Higashi, D. Kong, R. Abe, J. Tang, Mimicking natural photosynthesis: Solar to renewable H$_2$ fuel synthesis by Z-scheme water splitting systems, Chem. Rev. 118 (2018) 5201–5241.

[6] Z. Wang, C. Li, K. Domen, Recent developments in heterogeneous photocatalysts for solar-driven overall water splitting, Chem. Soc. Rev. 48 (2019) 2109–2125.

[7] G. Ling, S. Ng, W. Ong, Tailor-engineered 2D cocatalysts: Harnessing electron–hole redox center of 2D g-C$_3$N$_4$ photocatalysts toward solar-to-chemical conversion and environmental purification, Adv. Funct. Mater. 32 (2022) 2111875.

[8] J. Xu, J. Thomas, C. Laurent, N. Dieter, A. Markus, S. Menny, Liquid-based growth of polymeric carbon nitride layers and their use in a mesostructured polymer solar cell with V oc exceeding 1 V, J. Am. Chem. Soc. 136 (2014) 13486–13489.

[9] W. Ong, L. Tan, Y. Ng, S. Yong, S. Chai, Graphitic carbon nitride (g-C$_3$N$_4$)-based photocatalysts for artificial photosynthesis and environmental remediation: Are we a step closer to achieving sustainability?, Chem Rev. 116 (2016) 7159–7329.

[10] C. Cheng, L. Mao, J. Shi, F. Xue, S. Zong, B. Zheng, L. Guo, NiCo$_2$O$_4$ nanosheets as a novel oxygen-evolution-reaction cocatalyst in situ bonded on the g-C$_3$N$_4$ photocatalyst for excellent overall water splitting, J. Mater. Chem. A 9 (2021) 12299–12306.

[11] L. Zhou, J. Lei, F. Wang, L. Wang, M. Hoffmann, Y. Liu, S. In, J. Zhang, Carbon nitride nanotubes with in situ grafted hydroxyl groups for highly efficient spontaneous H$_2$O$_2$ production, Appl. Catal. B: Environ. 288 (2021) 119993.

[12] H. Yu, R. Shi, Y. Zhao, T. Bian, Y. Zhao, C. Zhou, G. Waterhouse, L. Wu, C. Tung, T. Zhang, Alkali-assisted synthesis of nitrogen deficient graphitic carbon nitride with tunable band structures for efficient visible-light-driven hydrogen evolution, Adv. Mater. 29 (2017) 1605148.

[13] C. Cheng, J. Shi, L. Wen, C.-L. Dong, Y.-C. Huang, Y. Zhang, S. Zong, Z. Diao, S. Shen, L. Guo, Disordered nitrogen-defect-rich porous carbon nitride photocatalyst for highly efficient H$_2$ evolution under visible-light irradiation, Carbon 181 (2021) 193–203.

[14] Z. Tong, D. Yang, Y. Sun, Y. Nan, Z. Jiang, Tubular g-C$_3$N$_4$ isotype heterojunction: enhanced visible-light photocatalytic activity through cooperative manipulation of oriented electron and hole transfer, Small 12 (2016) 4093–4101.

[15] C. Cheng, C. Dong, J. Shi, L. Mao, Y. Huang, X. Kang, S. Zong, S. Shen, Regulation on polymerization degree and surface feature in graphitic carbon nitride towards efficient photocatalytic H$_2$ evolution under visible-light irradiation, J. Mater. Sci. Technol. 98 (2022) 160–168.

[16] S. An, Y. Guo, X. He, P. Gao, G. Hou, J. Hou, C. Song, X. Guo, Intermediate-induced repolymerization for constructing self-assembly architecture: Red crystalline carbon nitride nanosheets for notable hydrogen evolution, Appl. Catal. B: Environ. 310 (2022) 121323.

[17] H. Dong, X. Guo, C. Yang, Z. Ouyang, Synthesis of g-C$_3$N$_4$ by different precursors under burning explosion effect and its photocatalytic degradation for tylosin, Appl. Catal. B: Environ. 230 (2018) 65–76.

[18] Z. Yu, X. Yue, J. Fan, Q. Xiang, Crystalline intramolecular ternary carbon nitride homojunction for photocatalytic hydrogen evolution, ACS Catal. 12 (2022) 6345–6358.

[19] W. Luo, Y. Li, J. Wang, J. Liu, N. Zhang, M. Zhao, J. Wu, W. Zhou, L. Wang, Asymmetric structure engineering of polymeric carbon nitride for visible-light-driven reduction reactions, Nano Energy 87 (2021) 106168.

[20] V. Lau, V. Yu, F. Ehrat, T. Botari, I. Moudrakovski, T. Simon, V. Duppel, E. Medina, J. Stolarczyk, J. Feldmann, V. Blum, B. Lotsch, Urea-modified carbon nitrides: Enhancing photocatalytic hydrogen evolution by rational defect engineering, Adv. Energy Mater. 7 (2017) 1602251.

[21] D. Martin, K. Qiu, S. Shevlin, A. Handoko, X. Chen, Z. Guo, J. Tang, Highly efficient photocatalytic H$_2$ evolution from water using visible light and structure-controlled graphitic carbon nitride, Angew. Chem. Int. Ed. 53 (2014) 9240–9245.

[22] D. Zhang, Y. Guo, Z. Zhao, Porous defect-modified graphitic carbon nitride via a facile one-step approach with significantly enhanced photocatalytic hydrogen evolution under visible light irradiation, Appl. Catal. B: Environ. 226 (2018) 1–9.

[23] B. Wu, L. Zhang, B. Jiang, Q. Li, C. Tian, Y. Xie, W. Li, H. Fu, Ultrathin porous carbon nitride bundles with an adjustable energy band structure toward simultaneous solar photocatalytic water splitting and selective phenylcarbinol oxidation, Angew. Chem. Int. Ed. 60 (2021) 4815–4822.

[24] Q. He, B. Viengkeo, X. Zhao, Z. Qin, J. Zhang, X. Yu, Y. Hu, W. Huang, Y. Li, Multiscale structural engineering of carbon nitride for enhanced photocatalytic H$_2$O$_2$ production, Nano Res. (2021) 1–7.

[25] Z. Mo, X. Zhu, Z. Jiang, Y. Song, D. Liu, H. Li, X. Yang, Y. She, Y. Lei, S. Yuan, H. Li, L. Song, Q. Yan, H. Xu, Porous nitrogen-rich g-C$_3$N$_4$ nanotubes for efficient photocatalytic CO$_2$ reduction, Appl. Catal. B: Environ. 256 (2019) 117854.

[26] Z. Mo, H. Xu, Z. Chen, X. She, Y. Song, J. Wu, P. Yan, L. Xu, Y. Lei, S. Yuan, H. Li, Self-assembled synthesis of defect-engineered graphitic carbon nitride nanotubes for efficient conversion of solar energy, Appl. Catal. B: Environ. 225 (2018) 154–161.

[27] Z. Chen, T. Fan, M. Shao, X. Yu, Q. Wu, J. Li, W. Fang, X. Yi, Simultaneously enhanced photon absorption and charge transport on a distorted graphitic carbon nitride toward visible light photocatalytic activity, Appl. Catal. B: Environ. 242 (2019) 40–50.

[28] P. Xia, P. Antonietti, B. Zhu, T. Heil, J. Yu, S. Cao, Designing defective crystalline carbon nitride to enable selective CO$_2$ photoreduction in the gas phase, Adv. Funct. Mater. 29 (2019) 1900093.

[29] Q. Han, Z. Cheng, B. Wang, H. Zhang, L. Qu, Significant enhancement of visible-light-driven hydrogen evolution by structure regulation of carbon nitrides, ACS Nano 12 (2018) 5221–5227.

[30] M. Wang, G. Zhong, L. Chen, Synthesis, optical characterization, and thermal decomposition of complexes based on biuret ligand, Int. J. Opt. 2016 (2016) 1–8.

[31] M. Factorovich, L. Guz, R. Candal, N-TiO$_2$: Chemical synthesis and photocatalysis, Adv. in Phys. Chem. 2011 (2011) 1–8.

[32] X. Wang, K. Maeda, A. Thomas, K. Takanabe, G. Xin, J. Carlsson, K. Domen, M. Antonietti, A metal-free polymeric photocatalyst for hydrogen production from water under visible light, Nat Mater. 8 (2009) 76–80.

[33] Y. Cui, G. Zhang, Z. Lin, X. Wang, Condensed and low-defected graphitic carbon nitride with enhanced photocatalytic hydrogen evolution under visible light irradiation, Appl. Catal. B: Environ. 181 (2016) 413–419.

[34] Y. Kang, Y. Yang, L.C. Yin, X. Kang, G. Liu, H.M. Cheng, An amorphous carbon nitride photocatalyst with greatly extended visible-light-responsive range for photocatalytic hydrogen generation, Adv. Mater. 27 (2015) 4572–4577.

[35] C. Cheng, L. Mao, Z. Huang, J. Shi, B. Zheng, Y. Zhang, L. Guo, Bridging regulation in graphitic carbon nitride for band-structure modulation and directional charge transfer towards efficient H2 evolution under visible-light irradiation, J. Colloid Interf. Sci. 601 (2021) 220–228.

[36] C. Cheng, S. Zong, J. Shi, F. Xue, Y. Zhang, X. Guan, B. Zheng, J. Deng, L. Guo, Facile preparation of nanosized MoP as cocatalyst coupled with g-C$_3$N$_4$ by surface bonding state for enhanced photocatalytic hydrogen production, Appl. Catalysis B: Environ. 265 (2020) 118620.

[37] C. Cheng, J. Shi, F. Du, S. Zong, X. Guan, Y. Zhang, M. Liu, L. Guo, Simply blending Ni nanoparticles with typical photocatalysts for efficient photocatalytic H2 production, Catal, Sci. Technol. 9 (2019) 7016–7022.

[38] B. Zhou, S. Ding, B. Zhang, L. Xu, R. Chen, L. Luo, W. Huang, Z. Xie, A. Pan, G. Huang, Dimensional transformation and morphological control of graphitic carbon nitride from water-based supramolecular assembly for photocatalytic hydrogen evolution: from 3D to 2D and 1D nanostructures, Appl. Catal. B: Environ. 254 (2019) 321–328.

[39] H. Lan, L. Li, X. An, F. Liu, C. Chen, H. Liu, J. Qu, Microstructure of carbon nitride affecting synergetic photocatalytic activity: Hydrogen bonds vs. structural defects, Appl. Catal. B: Environ. 204 (2017) 49–57.

[40] J. Zhang, J. Sun, K. Maeda, K. Domen, P. Liu, M. Antonietti, X. Fu, X. Wang, Sulfur-mediated synthesis of carbon nitride: Band-gap engineering and improved functions for photocatalysis, Energy Environ. Sci. 4 (2011) 675–678.

[41] Y. Jun, E. Lee, X. Wang, W. Hong, G. Stucky, A. Thomas, From melamine-cyanuric acid supramolecular aggregates to carbon nitride hollow spheres, Adv. Funct. Mater. 23 (2013) 3661–3667.

[42] D. Zhao, J. Chen, C. Dong, W. Zhou, Y. Huang, S.S. Mao, L. Guo, S. Shen, Interlayer interaction in ultrathin nanosheets of graphitic carbon nitride for efficient photocatalytic hydrogen evolution, J. Catal. 352 (2017) 491–497.

[43] D. Zhao, C. Dong, B. Wang, C. Chen, Y. Huang, Z. Diao, S. Li, L. Guo, S. Shen, Synergy of dopants and defects in graphitic carbon nitride with exceptionally modulated band structures for efficient photocatalytic oxygen evolution, Adv. Mater. 31 (2019) 1903545.

[44] F. Xu, B. Zhu, B. Cheng, J. Yu, J. Xu, 1D/2D TiO_2/MoS_2 hybrid nanostructures for enhanced photocatalytic CO_2 reduction, Adv. Opt. Mater. 23 (2018) 1800911.

[45] J. Ji, J. Wen, Y. Shen, Y. Lv, Y. Chen, S. Liu, H. Ma, Y. Zhang, Simultaneous noncovalent modification and exfoliation of 2D carbon nitride for enhanced electrochemiluminescent biosensing, J. Am. Chem. Soc. 139 (2017) 11698–11701.

[46] F. Xu, J. Zhang, B. Zhu, J. Yu, J. Xu, $CuInS_2$ sensitized TiO_2 hybrid nanofibers for improved photocatalytic CO_2 reduction, Appl. Catal. B: Environ. 230 (2018) 194–202.

[47] Y. Li, B. Zhou, H. Zhang, T. Huang, Y. Wang, W. Huang, W. Hu, A. Pan, X. Fan, G. Huang, A host–guest self-assembly strategy to enhance π-electron densities in ultrathin porous carbon nitride nanocages toward highly efficient hydrogen evolution, Chem. Eng. J. 430 (2022) 132880.

[48] G. Liu, T. Wang, H. Zhang, X. Meng, D. Hao, K. Chang, P. Li, T. Kako, J. Ye, Nature-inspired environmental "phosphorylation" boosts photocatalytic H_2 production over carbon nitride nanosheets under visible-light irradiation, Angew. Chem. Int. Ed. 54 (2015) 13561–13565.

[49] C. Wu, S. Xue, Z. Qin, M. Nazari, G. Yang, S. Yue, T. Tong, H. Ghasemi, F. Hernandez, S. Xue, D. Zhang, H. Wang, Z. Wang, S. Pu, J. Bao, Making g-C_3N_4 ultra-thin nanosheets active for photocatalytic overall water splitting, Appl. Catal. B: Environ. 282 (2021) 119557.

[50] Y. Li, D. Zhang, J. Fan, Q. Xiang, Highly crystalline carbon nitride hollow spheres with enhanced photocatalytic performance, Chinese, J. Catal. 42 (2021) 627–636.